Improving estimates of the cerebral metabolic rate of oxygen from optical imaging data.

Matthew J.P. Barrett[1,†], Vinod Suresh[1,2]

[1]Auckland Bioengineering Institute, The University of Auckland
[2]Department of Engineering Science, The University of Auckland

[†]Present address and address for correspondence:
Dr Matthew Barrett
Institute of Pharmacology and Toxicology
University of Zürich
Winterthurerstrasse 190
CH-8057 Zürich
SWITZERLAND
Phone: +41 44 635 6087
Fax: +41 44 635 68 57
Email: mbarrett@pharma.uzh.ch

Abstract

The cerebral metabolic rate of oxygen ($CMRO_2$) is an important measure of brain function. Since it is challenging to measure directly, especially dynamically, a number of neuroimaging techniques aim to infer activation-induced changes in $CMRO_2$ from indirect data. Here, we employed a mathematical modelling approach, based on fundamental biophysical principles, to investigate the validity of the widely-used method to calculate $CMRO_2$ from optical measurements of cerebral blood flow and haemoglobin saturation. Changes in $CMRO_2$ calculated in this way differed substantially from the changes in $CMRO_2$ directly imposed on the model, in model-only simulations and simulations of *in vivo* data under both steady state and dynamic conditions. These results suggest that the assumptions underlying the calculation method are not appropriate, and that it is important to take into account, under steady state conditions: 1) the presence of deoxyhaemoglobin in arteriolar vessels; and 2) blood volume changes, especially in veins. Under dynamic conditions, the model predicted that calculated changes in $CMRO_2$ are moderately correlated with the rate of oxygen extraction – not consumption – during the initial phase of stimulation. However, during later phases of stimulation the calculation is dominated by the change in blood flow. We propose that a more sophisticated approach is required to estimate $CMRO_2$ changes from these types of data.

Keywords

Cerebral blood flow, energy metabolism, mathematical modelling, neurovascular coupling, optical imaging

1 Introduction

The cerebral metabolic rate of oxygen ($CMRO_2$), which represents the rate at which oxygen is consumed to meet the energy demands of the working brain, is an important measure of neural activity in health and disease. However, there are many aspects of the metabolic changes that are caused by variations in neuronal activity which are not fully understood; for example, the nature of the cellular energy pathways which drive the increased demand, the relative magnitude of the metabolic changes compared with changes in blood flow, and the evolutionary advantage conferred by this process remain unclear (Attwell et al., 2010; Buxton, 2010; Fox, 2012; Pellerin and Magistretti, 2012). Better knowledge of this fundamental process is vital to improve our understanding of basic neuronal function. In addition, it may also enable more accurate, and perhaps even quantitative interpretation of non-invasive neuroimaging modalities such as functional Magnetic Resonance Imaging (fMRI) using the Blood Oxygenation Level Dependent (BOLD) signal.

Part of the uncertainty that surrounds neural metabolism is likely caused by the difficulty in measuring $CMRO_2$ directly. For example, steady-state measurements of $CMRO_2$ with PET require three separate scans, each with different oxygen-15 labelled tracers (Mintun et al., 1984). However, the measurements still rely on the assumption that there is no back flux of oxygen from tissue to the vasculature, and require a model to interpret the effects of CBF, $CMRO_2$ and CBV (cerebral blood volume) on the observed tracer kinetics (Buxton, 2010; Mintun et al., 1984).

Steady-state $CMRO_2$ can also be measured using several magnetic resonance spectroscopy techniques following inhalation of oxygen-17 labelled O_2 gas (e.g. Mellon et al., 2009; Zhu et al., 2013). These approaches have a number of advantages, particularly the

ability to distinguish between oxygen that has not been metabolised (i.e. O_2) and that has (i.e. H_2O). However, measurements using these techniques are not yet widespread due to the high cost of oxygen-17 and difficulties in extending the approach to larger animals (Buxton, 2010; Zhu and Chen, 2011).

Dynamic measurements of $CMRO_2$ during neuronal activation are even more complicated, since the increase in $CMRO_2$ (i.e. O_2 demand) is confounded by a larger, concomitant increase in cerebral blood flow (CBF, i.e. O_2 supply). This phenomenon is often referred to as 'uncoupling' of CBF and $CMRO_2$ (Fox and Raichle, 1986). It is also possible to qualitatively estimate changes in $CMRO_2$ independently of CBF using flavoprotein autofluorescence imaging (FAI, Vazquez et al., 2012; Weber et al., 2004), although it is not clear how to relate the measured change in fluorescence to quantitative changes in $CMRO_2$.

Therefore, because of the technical challenges and relatively poor temporal resolution of the direct approaches, many studies aim to infer dynamic changes in $CMRO_2$ indirectly using an imaging modality sensitive to oxygenation, such as optical imaging (Dunn et al., 2005; Jones et al., 2001; Mayhew et al., 2000) or BOLD-fMRI (Davis et al., 1998; Hoge et al., 1999; Hyder et al., 2010; Mandeville et al., 1999). These techniques require a framework to convert a signal that represents oxygen *concentration* into a metric that represents the *rate* of oxygen *consumption*. The approaches considered here rely on Fick's principle, which states that the amount of oxygen extracted from the blood is proportional to CBF and the arterio-venous oxygenation difference. We contend that these methods are limited by two assumptions.

First, the approaches explicitly or implicitly assume that $CMRO_2$ is proportional to O_2 extraction, which may be normalised and referred to as the oxygen extraction fraction or OEF (Davis et al., 1998; Dunn et al., 2005; Hoge et al., 1999; Jones et al., 2001; Mandeville et al.,

1999; Mayhew et al., 2000). Under steady state conditions, $CMRO_2$ and O_2 extraction are matched, as tissue oxygen partial pressure (PO_2) does not vary significantly through time (Russell et al., 2012). This steady-state coupling may be an important regulator of metabolism or vascular development, since capillary density is strongly correlated with the activity of the metabolic enzyme cytochrome oxidase (Weber et al., 2008), in addition to CBF and cerebral glucose consumption (Klein et al., 1986).

However, O_2 extraction and $CMRO_2$ are not necessarily matched under dynamic conditions. A number of studies have reported a robust increase in tissue PO_2 following neural activation (Masamoto et al., 2008; Thompson et al., 2003; Vazquez et al., 2010), suggesting that the O_2 extracted from the blood may not be consumed immediately, i.e. transient changes in O_2 extraction exceed changes in $CMRO_2$. Therefore, we propose that it is inappropriate to use O_2 extraction as a proxy for $CMRO_2$ outside of steady state conditions.

Secondly, many of the approaches assume complete saturation of haemoglobin in arteries (Davis et al., 1998; Dunn et al., 2005; Hoge et al., 1999; Jones et al., 2001; Mandeville et al., 1999; Mayhew et al., 2000). However, more recent evidence suggests that the small arteries which supply individual cortical regions contain non-negligible levels of deoxyhaemoglobin (Kasischke et al., 2011; Yaseen et al., 2011), and this is likely to be even more significant under free breathing conditions without supplied oxygen (Vovenko, 1999). In addition, vascular PO_2 measurements imply that the saturation of cerebral arteries may change during neural activation, albeit by a relatively small amount (Vazquez et al., 2010).

In this study, we investigate the validity of these approaches using a predictive mathematical model. Rather than assuming $CMRO_2$ and O_2 extraction are equivalent, the model treats $CMRO_2$ as a tissue 'oxygen sink', in which oxygen is irreversibly consumed by the mitochondria during aerobic respiration. Then, we model oxygen extraction

independently, using a mass balance approach, where net O_2 flux from blood to tissue is driven by the PO_2 gradient (i.e. Fick's first law). In addition, we do not assume complete saturation of arterial haemoglobin, and instead calculate the baseline oxygen saturation from *in vivo* measurements.

While the basic principles behind our approach extend to any oxygenation based signal, in this study we focus on the widely-used calculation of dynamic $CMRO_2$ changes from optical measurements of haemoglobin (Dunn et al., 2005; Jones et al., 2001; Mayhew et al., 2000). Initially, we compare the existing calculation method to our proposed approach using model only simulations, and then we apply both methods to a published set of *in vivo* data (Jones et al., 2002).

2 Materials and methods

The blood flow and oxygen transport models used here have been described in detail previously (Barrett and Suresh, 2013; Barrett et al., 2012), but a summary of the theory and principal equations is given below. Table 1 contains a list of dynamic variables used in the model, and Supplementary Table 1 contains a list of the parameters. Similar to other models (Huppert et al., 2007; Zheng et al., 2005) we represent the complex cerebrovascular network as four lumped compartments: arteries, capillaries, veins, and tissue. These are referred to by the subscripts 1, 2, 3, and *t* respectively. The subscripts 0 and 4 refer to unmodelled larger arterial and venous compartments. Continuing a previous convention, variables in upper case are absolute quantities, while those in lower-case are dimensionless. The superscript * (e.g. $cmr_{O_2}^*$) represents a steady state value, typically at baseline.

2.1 Blood flow model

The model of fluid dynamics predicts changes in CBF and CBV in response to functional activation. Since the signalling pathways responsible for neurovascular coupling remain unclear (Attwell et al., 2010), in the model these changes are driven by an empirical vasodilatory stimulus which reduces arterial compliance and induces arterial dilation. The model generates predictions consistent with *in vivo* experimental measurements of CBF, CBV, blood vessel diameter and red blood cell velocity (Barrett et al., 2012).

The derivation and additional mathematical detail can be found in the original publication (Barrett et al., 2012), but briefly, the volume of blood within a vascular compartment i, $v_i(t)$, is conserved according to the equation

$$\frac{dv_i}{dt} = f_{i-1,i}(t) - f_{i,i+1}(t), \tag{1}$$

where $f_{i,j}(t)$ is the blood flow from compartment i to j. To conserve energy, the pressure at the entrance to each compartment, $p_i(t)$, can be written as

$$p_i(t) = \frac{1}{2} r_i(t) f_{i-1,i}(t) + \frac{v_i(t)}{c_i(t)}. \tag{2}$$

Here, the viscous resistance $r_i(t)$ is based on Poiseuille's law and depends on $v_i(t)$. The vascular compliance $c_i(t)$ incorporates the effects of volume stiffening, viscoelasticity and smooth muscle activation. Finally, the pressure drops across each compartment, $\Delta p_i(t)$, must sum to the total (reference) pressure drop, Δp_r, such that

$$\Delta p_r - \sum_{i=1}^{3} \Delta p_i(t) = 0. \tag{3}$$

With three vascular compartments, Equations (1)-(3) define a system of seven differential-algebraic equations in four flows and three volumes.

2.2 Oxygen transport model

The oxygen transport model couples to the model of fluid dynamics, and predicts changes in PO_2 and haemoglobin saturation (SO_2) in response to functional activation. Since the pathways responsible for neurovascular coupling are complex and remain uncertain (Attwell et al., 2010), changes in $CMRO_2$ are modelled using an empirical 'stimulus' applied to baseline $CMRO_2$. The model generates predictions consistent with *in vivo* experimental measurements of tissue and vascular PO_2 at baseline and during functional activation (Barrett and Suresh, 2013).

Further detail can be found in the original publication (Barrett and Suresh, 2013), but briefly, the amount of oxygen in each vascular compartment, $n_{O_2,i}(t)$, is conserved according to

$$\frac{dn_{O_2,i}}{dt} = f_{i-1,i}(t)c_{O_2,i-1,i}(t) - f_{i,i+1}(t)c_{O_2,i,i+1}(t) - j_{O_2,i}(t), \tag{4}$$

where $c_{O_2,i,j}(t)$ is the oxygen concentration of flow $f_{i,j}(t)$, and $j_{O_2,i}(t)$ is the flux of oxygen to tissue, which is defined from Fick's first law as

$$j_{O_2,i}(t) = g_i\left[\overline{p}_{O_2,i}(t) - \overline{p}_{O_2,t}(t)\right], \tag{5}$$

where g_i are oxygen conduction coefficients, $\overline{p}_{O_2,i}(t)$ is the mean vascular PO_2, and $\overline{p}_{O_2,t}(t)$ is the mean tissue PO_2. The amount of oxygen in the tissue compartment, $n_{O_2,t}(t)$, is conserved according to

$$\frac{dn_{O_2,t}}{dt} = \sum_{i=1}^{3} j_{O_2,i}(t) - cmr_{O_2}(t), \tag{6}$$

where $cmr_{O_2}(t)$, the $CMRO_2$ imposed on the model, is described mathematically in Appendix A.

For simplicity, we ignore the small fraction of oxygen dissolved in plasma and calculate input and output partial pressures using a Hill equation formulation to describe the oxygen-hemoglobin saturation curve, such that

$$p_{O_2,i,i+1}(t) = p_{50}\left[\frac{c_{O_2,max}}{c_{O_2,i,i+1}(t)} - 1\right]^{-\frac{1}{h}}, \tag{7}$$

where the constant p_{50} represents the PO_2 at which haemoglobin is 50% saturated, $c_{O_2,max}$ represents the maximum concentration of oxygen in whole blood, and h is the Hill exponent. In tissue, the average oxygen partial pressure, $\overline{p}_{O_2,t}(t)$, is calculated from Henry's law so

$$\overline{p}_{O_2,t}(t) = c_{O_2,t}(t) / \sigma_{O_2}, \tag{8}$$

where the constant σ_{O_2} represents the solubility of oxygen in tissue.

Assuming that haematocrit remains constant, the amount of haemoglobin, $n_{X,i}(t)$ (where $X \in \{HbT, HbO, dHb\}$), can be calculated such that

$$\begin{aligned} n_{HbT,i}(t) &= v_i(t), \\ n_{HbO,i}(t) &= v_i(t)s_{O_2,i}(t), \text{ and} \\ n_{dHb,i}(t) &= v_i(t)\left[1 - s_{O_2,i}(t)\right], \end{aligned} \tag{9}$$

where *HbT*, *HbO*, and *dHb*, correspond to total, oxy-, and deoxyhaemoglobin, and $s_{O_2,i}(t)$ is the oxygen saturation. Note that the dimensionless values above do not explicitly depend on the haematocrit, and the absolute level of haematocrit enters into the model only through its influence on $c_{O_2,max}$ in the Hill equation.

On the basis of recent experimental observations that observed oxygen flux from arterioles to venules (Lecoq et al., 2011) and increasing venous PO_2 values (Vazquez et al., 2010; Vovenko, 1999), the model also includes an arterio-venous diffusive shunt in addition to the other terms in Equation (4). The flux through the shunt, $j_{O_2,s}(t)$, is subtracted from the arterial and added to the venous compartments, and is calculated such that

$$j_{O_2,s}(t) = g_s\left[\,\overline{p}_{O_2,1}(t) - \overline{p}_{O_2,3}(t)\right], \tag{10}$$

where g_s is the shunt oxygen conduction coefficient.

Previous work from our group demonstrated that a dynamic increase in net capillary permeability, an effect that may be the result of functional recruitment, is necessary to obtain predictions consistent with the data (Barrett and Suresh, 2013). Therefore, we include this mechanism here, and allow capillary permeability to vary according to

$$g_2(t) = g_2^*\left(1 + k_{CapPerm}\left[\,f_{0,1}(t) - f^*\right]\right), \tag{11}$$

where the constants g_2^* and f^* represent values at baseline, and $k_{CapPerm}$ describes the magnitude of the change in capillary permeability for a given change in CBF.

For a total of three vascular and one tissue compartments, Equations (4) and (6) expand to four ordinary differential equations in four oxygen amounts, and can be solved using the flows and volumes predicted by the blood flow model.

2.3 Estimating $CMRO_2$

Under steady state conditions where the derivative terms equal zero, Equations (4) and (6) reduce to a statement of Fick's principle, and the rate of oxygen extraction from the blood, $e_{O_2}^*$, is equivalent to $cmr_{O_2}^*$ such that

$$e_{O_2}^* \equiv \sum_{i=1}^{3} j_{O_2,i}{}^* = cmr_{O_2}^* = f^* \left(c_{O_2,0,1}{}^* - c_{O_2,3,4}{}^* \right). \quad (12)$$

However, when the derivative terms in Equations (4) and (6) are non-zero, it is not valid to make Equation (12) dynamic; mathematically:

$$cmr_{O_2}(t) \neq \overline{f}(t)\left[c_{O_2,0,1}(t) - c_{O_2,3,4}(t) \right], \quad (13)$$

where $\overline{f}(t)$ is the dynamic mean blood flow and can be calculated as a weighted average such that

$$\overline{f}(t) = \sum_{i=1}^{3} v_i(t)\left[f_{i-1,i}(t) + f_{i,i+1}(t) \right] \Big/ 2\sum_{i=1}^{3} v_i(t). \quad (14)$$

However, as discussed in the introduction, many approaches (Davis et al., 1998; Dunn et al., 2005; Hoge et al., 1999; Jones et al., 2001; Mandeville et al., 1999; Mayhew et al., 2000) rely on the normalised form of Equation (13), subject to the additional assumption that

$$\frac{c_{O_2,0,1}(t) - c_{O_2,3,4}(t)}{c_{O_2,0,1}{}^* - c_{O_2,3,4}{}^*} \approx \frac{n_{dHb,3}(t)}{n_{dHb,3}{}^*}. \quad (15)$$

(Note, the left hand side of Equation (15) can be made mathematically equal to the right hand side subject to the additional assumptions $c_{O_2,0,1}(t) = 1$ and $v_3(t)/v_3^* = 1$.)

While Equations (13) and (15) are not strictly true in the physical sense, it is not clear whether the resulting $CMRO_2$ calculation is 'close enough' to be used as an approximation. Therefore, in order to quantify the error, we compared the following metrics calculated from model simulations:

$$\begin{aligned} \text{Imposed} &= cmr_{O_2}(t) \Big/ cmr_{O_2}^*, \\ \text{Extracted} &= \sum_{i=1}^{3} j_{O_2,i}(t) \Big/ \sum_{i=1}^{3} j_{O_2,i}{}^*, \text{ and} \\ \text{Calculated} &= \overline{f}(t) n_{dHb,3}(t) \Big/ f^* n_{dHb,3}{}^*, \end{aligned} \quad (16)$$

where ‘Imposed’ is the rate of oxygen consumption in the tissue that is directly imposed on the model and ‘Extracted’ is the rate of oxygen extracted from the vascular compartments in the model. In contrast, the ‘Calculated’ metric is the rate of oxygen consumption that would be calculated using the most common calculation approach (Davis et al., 1998; Dunn et al., 2005; Hoge et al., 1999; Jones et al., 2001; Mandeville et al., 1999; Mayhew et al., 2000). Although the calculated $CMRO_2$ metric was originally intended to act as a proxy for extracted $CMRO_2$, we hypothesised that there would be a significant discrepancy between these two metrics, and, importantly, between the imposed $CMRO_2$ and both other metrics.

2.4 Experimental design

This section gives an overview of the design of the numerical experiments, which were carried out in two stages.

Model only simulations: The first stage of simulations considered three illustrative scenarios that are representative of the *in vivo* situation under certain conditions, in order to characterise the behaviour of the model. The scenarios were: (1) an increase in CBF without any increase in $CMRO_2$ (similar to hypercapnic inhalation (Jones et al., 2002), but without any change in blood gas conditions, and with a more rapid onset and offset), (2) an increase in $CMRO_2$ without any increase in CBF (similar to stimulation under sodium nitroprusside application (Masamoto et al., 2008), but without any change in baseline CBF), and (3) an increase in both CBF and $CMRO_2$ (similar to functional activation).

***In vivo* spectroscopic data:** The second stage of simulations considered measurements of CBF and haemoglobin made by Jones and colleagues in response to 20 second electrical stimulation of vibrissae in rats (Jones et al., 2002). These simulations were performed to determine whether the results from the model only simulations persisted under conditions consistent with *in vivo* data. The measurements were made at four graded

stimulus intensities, so include a range of flow and haemoglobin values. First, we adjusted the model baseline conditions for the measured femoral artery PO_2 (94.4 mmHg, Jones et al., 2002), as per our previous work (Barrett and Suresh, 2013; details in the supplementary material of this reference). For each stimulus intensity independently, we then adjusted the vasodilatory stimulus to fit the model predictions of CBF to the observations (Barrett et al., 2012). Finally, we adjusted the $CMRO_2$ stimulus to minimise the error between the model predictions and experimental measurements of hemoglobin (oxy- and deoxyhaemoglobin simultaneously).

Spectroscopic measurements of haemoglobin use assumed baseline concentrations to calculate relative changes (Dunn et al., 2005; Jones et al., 2001; Mayhew et al., 2000). Therefore, in order to ensure the model predictions are comparable with the experimental data, we adjusted the predictions to use the same baseline conditions that were assumed in the experimental data. We calculated these adjusted predictions of relative change in haemoglobin calculation, $\Delta c_X^{\mathring{a}}(t)$, where $X \in \{HbO, dHb\}$, according to

$$\begin{aligned} \Delta c_{HbO}^{\mathring{a}}(t) &= \sum_{i=1}^{3}\left[n_{HbO,i}(t) - n_{HbO,i}^{*} \right] \Big/ s_{O_2}^{\mathring{a}} \sum_{i=1}^{3} n_{HbT,i}^{*} \\ \Delta c_{dHb}^{\mathring{a}}(t) &= \sum_{i=1}^{3}\left[n_{dHb,i}(t) - n_{dHb,i}^{*} \right] \Big/ \left(1 - s_{O_2}^{\mathring{a}}\right) \sum_{i=1}^{3} n_{HbT,i}^{*} \end{aligned} \tag{17}$$

where $s_{O_2}^{\mathring{a}}$ is the average baseline saturation assumed in the experimental data (50% in the data used here: Jones et al., 2002). Since the model predictions are non-dimensionalised and total haemoglobin concentration is assumed constant in the blood, we do not adjust the model predictions of total haemoglobin. Supplementary Figure 1 shows a comparison of the raw and adjusted dynamic model predictions, and Supplementary Figure 2 summarises the raw and adjusted predictions from all simulations in the sensitivity analysis.

2.5 Optimisation, parameter sensitivity, and data analysis

All optimization was implemented in MATLAB R2010a (The MathWorks Inc., Natick, MA) using either a constrained Nelder-Mead simplex (Lagarias et al., 1998) or trust-region-reflective (Coleman and Li, 1996) algorithm, with initial parameter values chosen from a uniform random distribution. We repeated each stage of optimisation with different initial guesses, typically more than four times, to ensure that the values converged to a true optimal solution, and used the best of these repeats.

For the simulations of *in vivo* conditions, we also conducted analyses to determine whether the model predictions were sensitive to the choice of key parameters. We independently perturbed each parameter by a representative amount, typically ±10% (see Supplementary Table 2), and repeated the appropriate optimization stage(s) in each case.

Raw experimental data were not available, so it was not possible to compare model predictions to the data directly using statistical methods. However, we used statistical tests to provide evidence of differences between model predictions, given some variation in the parameters. To test for statistically significant differences, we compared metrics (e.g. different types of $CMRO_2$ increases) from the simulations in the sensitivity analysis using either a t-test or a non-parametric Wilcoxon rank sum test, depending on the result of a Shapiro-Wilk normality test. Paired, two-tailed tests were used in all analyses unless specified otherwise, and results were considered significant for $P < 0.05$.

3 Results

3.1 Model-only simulations

Figure 1 shows the model predictions under three illustrative sets of conditions, and compares the $CMRO_2$ imposed on the model with the $CMRO_2$ calculated as per Equation (16). In the first scenario, where CBF increased but there was no $CMRO_2$ increase imposed on the model, the calculation predicted a substantial (~20%) increase in $CMRO_2$. Under the opposite conditions, where there was no CBF increase but a 10% increase in $CMRO_2$ imposed on the model, the calculation was much closer to the imposed $CMRO_2$, predicting an ~8% increase in $CMRO_2$. When the increases in both CBF and $CMRO_2$ were imposed on the model, the calculation predicted a larger (~30%) increase in $CMRO_2$ than the simulation with CBF increase alone. The $CMRO_2$ extracted from the blood to tissue differed from the imposed $CMRO_2$ during periods of rapid change, such as during onset and offset of stimulation, but tended toward the imposed $CMRO_2$ as the conditions approached steady state, such as toward the end of the 20 second stimulation period (Figure 1B). The predictions of haemoglobin (Figure 1C) and tissue PO_2 (Figure 1D) appeared reasonable and consistent with the conditions imposed on the model.

3.2 Simulations of *in vivo* data

Figure 2 shows the optimal model predictions of CBF (Figure 2A), haemoglobin (Figure 2B-D), and tissue PO_2 (Figure 2E) fit to *in vivo* data obtained by Jones and colleagues (Jones et al., 2002). In general, the model predictions of CBF were a good fit to the data, although the model was unable to capture some of the more complex dynamics of the CBF data in response to 1.6 mA stimulation (Figure 2A). Therefore, although the CBF predictions would have been unlikely to cause major errors, they may have had a small impact on the dynamics of the other predictions at 1.6 mA stimulation. The model predictions of total haemoglobin

were generally consistent with the data, although had a slight tendency to predict larger increases than the measured data (Figure 2C). This is unlikely to have had a significant impact on the predictions of oxygenation-related variables, since the oxygen transport model is not strongly affected by changes in total haemoglobin (effectively CBV). The model predictions of oxy- (Figure 2B) and deoxyhaemoglobin (Figure 2D) were generally a good fit to the data, although the predictions in response to 1.6 mA stimulation may have been influenced by the minor discrepancies between model predictions of CBF and the data. The model predictions of tissue PO_2 (Figure 2E) appeared reasonable and consistent with the measurements of other physiological variables.

Figure 3 compares predictions of the different estimates of $CMRO_2$ under the conditions shown in Figure 2. The $CMRO_2$ increase calculated from blood flow and haemoglobin differed significantly from the $CMRO_2$ increase imposed on the model across all stimulus intensities (all $P < 0.001$). There was also a small but significant difference between the increases in extracted and imposed $CMRO_2$ across all stimulus intensities except 1.6mA ($P < 0.001$). The parameters defining the imposed $CMRO_2$ increase are listed in Supplementary Table 3.

Figure 4 shows the global correlation, across all stimulus intensities, between calculated $CMRO_2$ and other state variables, separated by the stimulus phase. (The raw data used to calculate the correlation coefficients are plotted in Supplementary Figure 3, and correlation coefficients calculated separately for each stimulus intensity are shown in Supplementary Figure 4.) Across all stimulus phases, there was a weak correlation between calculated $CMRO_2$ and the $CMRO_2$ imposed on the model (Pearson coefficient $\rho < 0.4$). There was moderate correlation between calculated and extracted $CMRO_2$ during stimulation onset ($\rho = 0.66$), but weaker correlation during the plateau and offset phases ($\rho < 0.4$). There

was a weak to moderate correlation between calculated $CMRO_2$ and CBF during stimulus onset ($\rho = 0.41$), and a very strong correlation ($\rho > 0.95$) during the plateau and offset phases.

Figure 5 shows the predicted 'coupling' between increases in CBF and imposed $CMRO_2$ using the four stimulus intensities considered in this study. There was a very weak correlation between the increases in CBF and imposed $CMRO_2$ ($\rho < 0.15$), and the predicted coupling ratio *n* (=ΔCBF/ΔCMRO2, see Buxton, 2010) varied by nearly an order of magnitude across the four different stimulus intensities.

4 Discussion

In this study we used a mathematical modelling approach to investigate the validity of the widely-used method to calculate $CMRO_2$ from optical measurements of cerebral blood flow and haemoglobin saturation. We compared the $CMRO_2$ calculated in this way with the $CMRO_2$ directly imposed on the model and the rate of oxygen extraction from blood to tissue using both illustrative model-only simulations (Figure 1) and simulations under conditions consistent with *in vivo* data (Jones et al., 2002; see also Figures 2-5). The results showed that the calculated $CMRO_2$ differed substantially from the imposed $CMRO_2$ in terms of both the dynamic (Figures 1B and 3A) and steady-state changes (Figure 3B). In addition, despite the approach being derived from Fick's principle, which is used to estimate steady-state oxygen extraction, the calculated $CMRO_2$ correlated only moderately with the extracted $CMRO_2$ for most phases of stimulation (Figure 4). While the extracted $CMRO_2$ tended toward the imposed $CMRO_2$ as the conditions approached steady-state, there were important differences between these two metrics during periods of rapid change, such as stimulus onset and offset. This difference manifests as tissue PO_2 changes, which are observed experimentally (Masamoto et al., 2008; Thompson et al., 2003; Vazquez et al., 2010). Therefore, we suggest

that the widely-used calculation method based on measurements of CBF and haemoglobin is not sufficient to provide an accurate estimate of the underlying $CMRO_2$, and that a more sophisticated approach is required. In addition, we suggest that oxygen extraction is not an appropriate proxy for $CMRO_2$ outside of steady-state conditions.

4.1 Estimating $CMRO_2$ using a model-based approach

While it is not possible to validate our model predictions of dynamic $CMRO_2$ definitively without data from a 'gold standard' measurement technique, we believe the model represents a substantial improvement on the existing calculation method for four primary reasons.

First, as with previous models (Boas et al., 2008; Huppert et al., 2007; Huppert et al., 2009; Zheng et al., 2005), we make an explicit distinction between the rate of oxygen consumption in the tissue and the rate of oxygen extraction from the blood to the tissue. This ensures that the model estimates of $CMRO_2$ are not unduly influenced by the rapid changes in oxygen extraction which can be driven by either haemodynamic or metabolic changes. In addition, including the tissue compartment makes it possible for the model to describe the increases in tissue PO_2 that occur during neural activation (Masamoto et al., 2008; Thompson et al., 2003; Vazquez et al., 2010). The fact that the commonly-used calculation method does not account for this tissue PO_2 'buffer' is likely to be a major factor in the transient discrepancy between the calculated $CMRO_2$ and that imposed on the model, but is not likely to have a significant impact on the steady state results.

Secondly, on the basis of recent *in vivo* evidence (Kasischke et al., 2011; Yaseen et al., 2011), the model does not assume that the arteries and arterioles supplying regions of cortical tissue are completely saturated, and also allows oxygen flux from arteries to tissue. This ensures that all compartments relevant to blood flow and oxygen exchange are involved in estimating $CMRO_2$. To examine the effect of the assumption of complete saturation in

arteries further, the simulations in Figure 1 were repeated with the femoral artery PO_2 increased from the reference value (85.6 mmHg, Vovenko, 1999), to a value close to 100% saturation (180 mmHg). This change brought the steady-state calculated $CMRO_2$ approximately 50% closer to the imposed $CMRO_2$ compared with the simulations in Figure 1 (data not shown). Therefore, the assumption that arterial blood is completely saturated is likely to be a major factor in the steady-state discrepancy between the $CMRO_2$ imposed on the model and that calculated from the commonly-used approach. However, the remaining difference between calculated and imposed $CMRO_2$, resulting from venous volume changes (see next paragraph), is still significant. Therefore, even in situations where it is valid to assume that arterial blood is 100% saturated, such as fMRI data pooled over relatively large regions of interest, there is likely to be a substantial difference between the calculated $CMRO_2$ and that imposed on the model.

Thirdly, as described mathematically in Equation (15), the commonly-used calculation method also implicitly assumes that there are no changes in venous volume. While this assumption is likely to be valid for brief stimulation periods, recent *in vivo* evidence and previous modelling from our group suggests that significant venous volume changes occur in response to longer stimulation periods (Barrett et al., 2012; Chen and Pike, 2009; Chen and Pike, 2010; Drew and Kleinfeld, 2011). Therefore, ignoring these volume changes is likely to introduce a significant discrepancy into the steady-state calculated $CMRO_2$. This effect may also be important when pooling data from relatively large regions of interest, as is common in fMRI.

Finally, even ignoring any limitations in the derivation of the existing calculation methods, the practical implementations of these approaches are complicated by the need to assume or estimate *venous* deoxyhaemoglobin changes based on a signal made up of the

combined contributions of *all* vascular and tissue compartments (Dunn et al., 2005; Jones et al., 2001). This requirement introduces an additional layer of uncertainty into the approach, and has the potential to misattribute effects caused by the measurement modality to the underlying physiology. In contrast, the model explicitly describes the biophysical interactions between the arterial, capillary, venous, and tissue compartments, and the estimates of $CMRO_2$ are therefore based on the aggregated contributions of all compartments. In addition, it is possible to superimpose an 'observation model' (Huppert et al., 2007), which characterises the behaviour of a particular measurement modality, onto the biophysical model.

To our knowledge, this is the first study which directly compares estimates of $CMRO_2$ calculated from measurements of CBF and haemoglobin to those predicted by a validated biophysical model. Huppert and colleagues (Huppert et al., 2007; Huppert et al., 2009) developed a similar model which estimated dynamic changes in $CMRO_2$ using data from a range of imaging modalities; however, the study considered only brief (<2 s) neural activation tasks, and did not compare the model predictions of $CMRO_2$ to those that would be calculated from the data with the commonly-used approach. Another compelling report from the same group (Boas et al., 2008) introduced a spatial component to explore the dynamics in both locally activated and surrounding regions; however, the activation task was also brief, and the report did not compare model-predicted $CMRO_2$ with calculated. In an earlier model, Zheng and colleagues (Zheng et al., 2005) did consider data from more extended stimulation (20 s), but did not report the dynamic $CMRO_2$ increases imposed on the model to produce fits to the data.

The model is a powerful tool to investigate neurovascular physiology, but it has certain limitations. Some of these limitations, such as the assumption of well-mixed

compartments, and assuming there is no delay in transport between compartments, have been discussed in more detail previously (Barrett and Suresh, 2013; Barrett et al., 2012). In addition, although there are a number of noteworthy spatial models that are developing the capability to explore the more complex interactions between structure and function (Fang et al., 2008; Lorthois et al., 2011; Reichold et al., 2009), reducing the complex cerebrovascular network to four dimensionless compartments is an approach which makes the model sufficiently tractable to consider the dynamics of bulk mechanisms in detail.

In this study, we assumed that the model predictions accurately represented physiological variables that were not directly measured, such as venous deoxyhaemoglobin levels. While it is not possible to prove the validity of the predictions in the case of this particular set of data, both the blood flow (Barrett et al., 2012) and oxygen transport (Barrett and Suresh, 2013) models have previously been successfully validated by comparing model predictions to independent data sources that were not used in any fitting. In particular, we previously reported model predictions consistent with *in vivo* measurements of arterial and venous PO_2 in response to forepaw stimulation (Barrett and Suresh, 2013). Given the strong similarities between the experimental conditions considered here and previously, this validation suggests that the model is likely to provide reasonable estimates of the underlying physiology here.

Finally, since not all of the parameters required for the model were directly measured during the experiment, it was necessary to use values from the literature in some cases. However, to ensure that the model predictions were not unduly sensitive to the choice of parameters, we conducted a sensitivity analysis whereby we modified the values of key parameters and repeated the simulations (see Supplementary Table 2). The results demonstrated that the substantial differences between the calculated and imposed $CMRO_2$

were not influenced by a reasonable degree of variation in the parameters. This also suggests that the findings here should remain valid even if there was some error in the measurement or selection of parameters.

4.2 Implications for $CMRO_2$ calculations from BOLD-fMRI

This study investigated a widely used method to calculate $CMRO_2$ from optical measurements, but it also has implications for related techniques, such as calibrated BOLD-fMRI. There are many similarities between the optical and MRI approach, since both signals depend on deoxygenated haemoglobin, and both $CMRO_2$ calculation methods rely on similar biophysical assumptions (Davis et al., 1998; Dunn et al., 2005; Hoge et al., 1999; Jones et al., 2001; Mandeville et al., 1999; Mayhew et al., 2000). However, partly because of the more complex nature of the BOLD signal and imaging process, MRI experiments often include an additional calibration experiment that is not normally performed in optical studies. The most common approach uses mild hypercapnia to induce an increase in CBF. On the assumption that there is no change in $CMRO_2$, this makes it possible to calibrate the magnitude of the observed BOLD signal change for a given change in CBF using a relatively simple biophysical model that combines a number of image acquisition and baseline physiological values into a single scaling parameter, normally M (Davis et al., 1998; Hoge et al., 1999).

The calibration experiment improves the accuracy of steady state $CMRO_2$ estimates from this type of data, since many of the sources of uncertainty are captured in the parameter M, which can be measured for each subject and/or imaging session. However, the accuracy of the results is nonetheless limited by the validity of the assumptions underlying the biophysical model. For example, there is evidence that hypercapnia at the level normally used in calibration experiments can cause a decrease in $CMRO_2$ (Kliefoth et al., 1979; Xu et al., 2011; Zappe et al., 2008), which would lead to systematic errors in the predictions of

activation-induced $CMRO_2$ (Griffeth and Buxton, 2011). In addition, incorrect estimates of the baseline distribution of or changes in blood volume have a similar effect (Griffeth and Buxton, 2011). Finally, since the widely-used biophysical models also implicitly assume that $CMRO_2$ is equal to oxygen extraction (Davis et al., 1998; Hoge et al., 1999), our results suggest that it may not be valid to use these models to predict dynamic changes in $CMRO_2$. Therefore, the modelling approach from this study will be applied to investigate the calculation of dynamic $CMRO_2$ from BOLD-fMRI data in future work.

4.3 Physiological implications of the improved $CMRO_2$ estimates

Although a detailed investigation of the coupling between blood flow and metabolism was not the focus of this study, the estimates of $CMRO_2$ predicted by our model may have relevant physiological implications. In particular, the fact that the coupling ratios predicted here varied by nearly an order of magnitude across the four stimulus intensities is somewhat unexpected, given that coupling ratios reported from fMRI and PET data appear more consistent (c.f. Figure 5 in this study with Figure 3 in Buxton, 2010).

There are plausible physiological hypotheses which could contribute to the actual or apparent variation in coupling ratios. First, as recently proposed by Buxton et al. (2014), the CBF and $CMRO_2$ response may be affected in different ways by excitatory and inhibitory neural activity. For example, increasing stimulus intensity is likely to increase both excitatory and inhibitory activity; however, if inhibitory activity has a stronger effect on increasing the CBF response than the $CMRO_2$ response, then increases in stimulus intensity would lead to increases in the coupling ratio. This hypothesis is consistent with a recent calibrated BOLD study in the visual cortex (Liang et al., 2013). In the case of an extremely strong stimulus, the high level of inhibitory activity could even start to decrease the magnitude of the $CMRO_2$ response while simultaneously increasing the CBF response.

Second, as discussed in more detail by Buxton (2010), the coupling ratio may vary between different cortical (and subcortical) regions. Third, the CBF and $CMRO_2$ responses may have different spatial extents or profiles, which could make the calculation of the coupling ratio dependent on the selection of the region of interest. This hypothesis is consistent with observations of the spatial variation in haemoglobin and arterial diameter response (Devor et al., 2007); however, we are not aware of any corresponding spatial measurements of $CMRO_2$, although the same study did observe spatial variation in cellular electrical activity using voltage sensitive dye and electrode arrays (Devor et al., 2007).

Finally, the coupling between the CBF and $CMRO_2$ response may vary through different cortical layers. Such a mechanism is plausible given that the responses of arterial diameter (Tian et al., 2010), BOLD-fMRI (Goense et al., 2012; Tian et al., 2010), electrophysiological signals (Devor et al., 2007; Li et al., 2011), and tissue PO_2 (Li et al., 2011) vary with cortical depth, as does the baseline activity of the oxidative metabolic enzyme cytochrome oxidase (Weber et al., 2008). Any physiological variation through cortical layers is particularly relevant for results obtained from optical imaging techniques, since their sensitivity typically decreases with cortical depth (Tian et al., 2011).

There are also a number of sources of variation between studies that estimate $CMRO_2$, a fact which may confound meaningful comparison of the coupling ratio. For example, there are differences in: the measurement modality (e.g. PET, BOLD-fMRI, optical techniques); stimulus nature (e.g. visual, electrical, air puff); stimulus intensity; species (e.g. animal, human); surgical preparation (e.g. cranial window, thinned skull, intact); ventilation (e.g. artificial ventilation, free breathing); and anaesthesia (e.g. urethane, alpha-chloralose, awake). These differences are all the more important since baseline conditions are thought to influence the magnitude of the vascular and metabolic response to activation (Buxton, 2010).

In order to test the ability of these hypotheses to explain the substantial variation in coupling ratio within and between experiments, a wider range of *in vivo* data involving different cortical regions and different types of neural activation are needed. Our results suggest that techniques more sophisticated than the existing calculation methods, like the model-based approach we use in this study, or other similar models (Dubeau et al., 2011; Huppert et al., 2007; Zheng et al., 2005), will be necessary to estimate increases in $CMRO_2$ from optical measurements, and dynamic increases in $CMRO_2$ from other oxygenation measurements.

5 Acknowledgments

M.B. acknowledges support from the Light Metals Research Centre during this research.

6 Conflict of Interest

The authors declare no conflict of interest.

References

Attwell, D., Buchan, A.M., Charpak, S., Lauritzen, M., MacVicar, B.A., Newman, E.A., 2010. Glial and neuronal control of brain blood flow. Nature 468, 232-243.

Barrett, M.J.P., Suresh, V., 2013. Extra permeability is required to model dynamic oxygen measurements: evidence for functional recruitment? Journal of Cerebral Blood Flow and Metabolism, 1-10.

Barrett, M.J.P., Tawhai, M.H., Suresh, V., 2012. Arteries dominate volume changes during brief functional hyperemia: Evidence from mathematical modelling. Neuroimage 62, 482 - 492.

Boas, D.A., Jones, S.R., Devor, A., Huppert, T.J., Dale, A.M., 2008. A vascular anatomical network model of the spatio-temporal response to brain activation. Neuroimage 40, 1116 - 1129.

Buxton, R., 2010. Interpreting oxygenation-based neuroimaging signals: the importance and the challenge of understanding brain oxygen metabolism. Frontiers in Neuroenergetics 2.

Buxton, R.B., Griffeth, V.E.M., Simon, A.B., Moradi, F., 2014. Variability of the coupling of blood flow and oxygen metabolism responses in the brain: a problem for interpreting BOLD studies but potentially a new window on the underlying neural activity. Frontiers in Neuroscience 8.

Chen, J.J., Pike, G.B., 2009. BOLD-specific cerebral blood volume and blood flow changes during neuronal activation in humans. NMR in Biomedicine 22, 1054-1062.

Chen, J.J., Pike, G.B., 2010. MRI measurement of the BOLD-specific flow-volume relationship during hypercapnia and hypocapnia in humans. Neuroimage 53, 383 - 391.

Coleman, T.F., Li, Y., 1996. An interior trust region approach for nonlinear minimization subject to bounds. SIAM journal on optimization 6, 418-445.

Davis, T.L., Kwong, K.K., Weisskoff, R.M., Rosen, B.R., 1998. Calibrated functional MRI: Mapping the dynamics of oxidative metabolism. Proceedings of the National Academy of Sciences 95, 1834-1839.

Devor, A., Tian, P., Nishimura, N., Teng, I.C., Hillman, E.M.C., Narayanan, S.N., Ulbert, I., Boas, D.A., Kleinfeld, D., Dale, A.M., 2007. Suppressed Neuronal Activity and Concurrent Arteriolar Vasoconstriction May Explain Negative Blood Oxygenation Level-Dependent Signal. Journal of Neuroscience 27, 4452-4459.

Drew, P.J., Kleinfeld, D., 2011. Fluctuating and sensory-induced vasodynamics in rodent cortex extend arteriole capacity. Proceedings of the National Academy of Sciences of the United States of America 108, 8473-8478.

Dubeau, S., Desjardins, M., Pouliot, P., Beaumont, E., Gaudreau, P., Ferland, G., Lesage, F., 2011. Biophysical model estimation of neurovascular parameters in a rat model of healthy aging. Neuroimage 57, 1480-1491.

Dunn, A.K., Devor, A., Dale, A.M., Boas, D.A., 2005. Spatial extent of oxygen metabolism and hemodynamic changes during functional activation of the rat somatosensory cortex. Neuroimage 27, 279 - 290.

Fang, Q., Sakadžić, S., Ruvinskaya, L., Devor, A., Dale, A.M., Boas, D.A., 2008. Oxygen advection and diffusion in a three- dimensional vascular anatomical network. Opt. Express 16, 17530-17541.

Fox, P.T., 2012. The coupling controversy. Neuroimage 62, 594-601.

Fox, P.T., Raichle, M.E., 1986. Focal physiological uncoupling of cerebral blood flow and oxidative metabolism during somatosensory stimulation in human subjects. Proceedings of the National Academy of Sciences of the United States of America 83, 1140-1144.

Goense, J., Merkle, H., Logothetis, Nikos K., 2012. High-Resolution fMRI Reveals Laminar Differences in Neurovascular Coupling between Positive and Negative BOLD Responses. Neuron 76, 629-639.

Griffeth, V.E.M., Buxton, R.B., 2011. A theoretical framework for estimating cerebral oxygen metabolism changes using the calibrated-BOLD method: Modeling the effects of blood volume

distribution, hematocrit, oxygen extraction fraction, and tissue signal properties on the BOLD signal. Neuroimage 58, 198 - 212.
Hoge, R.D., Atkinson, J., Gill, B., Crelier, G.R., Marrett, S., Pike, G.B., 1999. Investigation of BOLD signal dependence on cerebral blood flow and oxygen consumption: The deoxyhemoglobin dilution model. Magnetic Resonance in Medicine 42, 849-863.
Huppert, T.J., Allen, M.S., Benav, H., Jones, P.B., Boas, D.A., 2007. A multicompartment vascular model for inferring baseline and functional changes in cerebral oxygen metabolism and arterial dilation. Journal of Cerebral Blood Flow and Metabolism 27, 1262-1279.
Huppert, T.J., Allen, M.S., Diamond, S.G., Boas, D.A., 2009. Estimating cerebral oxygen metabolism from fMRI with a dynamic multicompartment Windkessel model. Human Brain Mapping 30, 1548-1567.
Hyder, D.S.F., Sanganahalli, B.G., Herman, P., Coman, D., Maandag, N.J.G., Behar, K.L., Blumenfeld, H., Rothman, D.l., 2010. Neurovascular and neurometabolic couplings in dynamic calibrated fMRI: transient oxidative neuroenergetics for block-design and event-related paradigms. Frontiers in Neuroenergetics 2.
Jones, M., Berwick, J., Johnston, D., Mayhew, J., 2001. Concurrent Optical Imaging Spectroscopy and Laser-Doppler Flowmetry: The Relationship between Blood Flow, Oxygenation, and Volume in Rodent Barrel Cortex. Neuroimage 13, 1002 - 1015.
Jones, M., Berwick, J., Mayhew, J., 2002. Changes in Blood Flow, Oxygenation, and Volume Following Extended Stimulation of Rodent Barrel Cortex. Neuroimage 15, 474 - 487.
Kasischke, K.A., Lambert, E.M., Panepento, B., Sun, A., Gelbard, H.A., Burgess, R.W., Foster, T.H., Nedergaard, M., 2011. Two-photon NADH imaging exposes boundaries of oxygen diffusion in cortical vascular supply regions. Journal of Cerebral Blood Flow and Metabolism 31, 68-81.
Klein, B., Kuschinsky, W., Schrock, H., Vetterlein, F., 1986. Interdependency of local capillary density, blood flow, and metabolism in rat brains. American Journal of Physiology 251, H1333-1340.
Kliefoth, A.B., Grurb, R.L., Raichle, M.E., 1979. Depression of cerebral oxygen utilization by hypercapnia in the rhesus monkey. Journal of Neurochemistry 32, 661-663.
Lagarias, J.C., Reeds, J.A., Wright, M.H., Wright, P.E., 1998. Convergence Properties of the Nelder--Mead Simplex Method in Low Dimensions. SIAM journal on optimization 9, 112-147.
Lecoq, J., Parpaleix, A., Roussakis, E., Ducros, M., Houssen, Y.G., Vinogradov, S.A., Charpak, S., 2011. Simultaneous two-photon imaging of oxygen and blood flow in deep cerebral vessels. Nature Medicine 17, 893-898.
Li, J., Bravo, D.S., ..., McHugh, S.B., 2011. Rapid laminar-specific changes in tissue oxygen accompany localized neuronal activity in rat and mouse whisker-barrel cortex. European Journal of Neuroscience.
Liang, C.L., Ances, B.M., Perthen, J.E., Moradi, F., Liau, J., Buracas, G.T., Hopkins, S.R., Buxton, R.B., 2013. Luminance contrast of a visual stimulus modulates the BOLD response more than the cerebral blood flow response in the human brain. Neuroimage 64, 104-111.
Lorthois, S., Cassot, F., Lauwers, F., 2011. Simulation study of brain blood flow regulation by intra-cortical arterioles in an anatomically accurate large human vascular network: Part I: Methodology and baseline flow. Neuroimage 54, 1031-1042.
Mandeville, J.B., Marota, J.J., Ayata, C., Moskowitz, M.A., Weisskoff, R.M., Rosen, B.R., 1999. MRI measurement of the temporal evolution of relative CMRO2 during rat forepaw stimulation. Magnetic Resonance in Medicine 42, 944-951.
Masamoto, K., Vazquez, A., Wang, P., Kim, S.-G., 2008. Trial-by-trial relationship between neural activity, oxygen consumption, and blood flow responses. Neuroimage 40, 442 - 450.
Mayhew, J., Johnston, D., Berwick, J., Jones, M., Coffey, P., Zheng, Y., 2000. Spectroscopic Analysis of Neural Activity in Brain: Increased Oxygen Consumption Following Activation of Barrel Cortex. Neuroimage 12, 664-675.
Mellon, E.A., Beesam, R.S., Baumgardner, J.E., Borthakur, A., Witschey 2nd, W.R., Reddy, R., 2009. Estimation of the regional cerebral metabolic rate of oxygen consumption with proton detected 17O MRI during precision 17O2 inhalation in swine. Journal of Neuroscience Methods 179, 29-39.

Mintun, M.A., Raichle, M.E., Martin, W.R.W., Herscovitch, P., 1984. Brain Oxygen Utilization Measured with O-15 Radiotracers and Positron Emission Tomography. Journal of Nuclear Medicine 25, 177-187.
Pellerin, L., Magistretti, P.J., 2012. Sweet sixteen for ANLS. Journal of Cerebral Blood Flow and Metabolism 32, 1152-1166.
Reichold, J., Stampanoni, M., Lena Keller, A., Buck, A., Jenny, P., Weber, B., 2009. Vascular graph model to simulate the cerebral blood flow in realistic vascular networks. Journal of Cerebral Blood Flow and Metabolism 29, 1429-1443.
Russell, D.M., Garry, E.M., Taberner, A.J., Barrett, C.J., Paton, J.F.R., Budgett, D.M., Malpas, S.C., 2012. A fully implantable telemetry system for the chronic monitoring of brain tissue oxygen in freely moving rats. Journal of Neuroscience Methods 204, 242-248.
Thompson, J.K., Peterson, M.R., Freeman, R.D., 2003. Single-Neuron Activity and Tissue Oxygenation in the Cerebral Cortex. Science 299, 1070-1072.
Tian, P., Devor, A., Sakadžić, S., Dale, A.M., Boas, D.A., 2011. Monte Carlo simulation of the spatial resolution and depth sensitivity of two-dimensional optical imaging of the brain. Journal of Biomedical Optics 16, 016006-016006.
Tian, P., Teng, I.C., May, L.D., Kurz, R., Lu, K., Scadeng, M., Hillman, E.M.C., De Crespigny, A.J., D'Arceuil, H.E., Mandeville, J.B., Marota, J.J.A., Rosen, B.R., Liu, T.T., Boas, D.A., Buxton, R.B., Dale, A.M., Devor, A., 2010. Cortical depth-specific microvascular dilation underlies laminar differences in blood oxygenation level-dependent functional MRI signal. Proceedings of the National Academy of Sciences of the United States of America 107, 15246-15251.
Vazquez, A.L., Fukuda, M., Kim, S.-G., 2012. Evolution of the dynamic changes in functional cerebral oxidative metabolism from tissue mitochondria to blood oxygen. Journal of Cerebral Blood Flow and Metabolism 32, 745-758.
Vazquez, A.L., Fukuda, M., Tasker, M.L., Masamoto, K., Kim, S.-G., 2010. Changes in cerebral arterial, tissue and venous oxygenation with evoked neural stimulation: implications for hemoglobin-based functional neuroimaging. Journal of Cerebral Blood Flow and Metabolism 30, 428-439.
Vovenko, E., 1999. Distribution of oxygen tension on the surface of arterioles, capillaries and venules of brain cortex and in tissue in normoxia: an experimental study on rats. Pflugers Archiv. European Journal of Physiology 437, 617-623.
Weber, B., Burger, C., Wyss, M.T., Von Schulthess, G.K., Scheffold, F., Buck, A., 2004. Optical imaging of the spatiotemporal dynamics of cerebral blood flow and oxidative metabolism in the rat barrel cortex. European Journal of Neuroscience 20, 2664-2670.
Weber, B., Keller, A.L., Reichold, J., Logothetis, N.K., 2008. The Microvascular System of the Striate and Extrastriate Visual Cortex of the Macaque. Cereb. Cort. 18, 2318-2330.
Xu, F., Uh, J., Brier, M.R., Hart, J., Jr., Yezhuvath, U.S., Gu, H., Yang, Y., Lu, H., 2011. The influence of carbon dioxide on brain activity and metabolism in conscious humans. Journal of Cerebral Blood Flow and Metabolism 31, 58-67.
Yaseen, M.A., Srinivasan, V.J., Sakadzic, S., Radhakrishnan, H., Gorczynska, I., Wu, W., Fujimoto, J.G., Boas, D.A., 2011. Microvascular oxygen tension and flow measurements in rodent cerebral cortex during baseline conditions and functional activation. Journal of Cerebral Blood Flow and Metabolism 31, 1051-1063.
Zappe, A.C., UludaÄŸ, K., Oeltermann, A., UÄŸurbil, K., Logothetis, N.K., 2008. The Influence of Moderate Hypercapnia on Neural Activity in the Anesthetized Nonhuman Primate. Cerebral Cortex 18, 2666-2673.
Zheng, Y., Johnston, D., Berwick, J., Chen, D., Billings, S., Mayhew, J., 2005. A three-compartment model of the hemodynamic response and oxygen delivery to brain. Neuroimage 28, 925 - 939.
Zhu, X.-H., Chen, J.M., Tu, T.-W., Chen, W., Song, S.-K., 2013. Simultaneous and noninvasive imaging of cerebral oxygen metabolic rate, blood flow and oxygen extraction fraction in stroke mice. Neuroimage 64, 437-447.
Zhu, X.-H., Chen, W., 2011. In vivo oxygen-17 NMR for imaging brain oxygen metabolism at high field. Progress in Nuclear Magnetic Resonance Spectroscopy 59, 319-335.

Appendix A: CMRO2 Stimulus

The $CMRO_2$ imposed on the model, $cmr_{O_2}(t)$, is a simplified form of that presented in Barrett and Suresh (2013), such that

$$cmr_{O_2}(t) = cmr^*_{O_2}\left[1 + s_t(t)\right], \tag{A.1}$$

where the constant $cmr^*_{O_2}$ is the baseline rate of oxygen consumption. The empirical stimulus term, $s_t(t)$, is described by

$$s_t(t) = \begin{cases} s_{up}(t), & t < t_0 + \tau_{up} \\ s^*(t), & t_0 + \tau_{up} \le t \le t_0 + t_{stim} \\ s_{down}(t), & t > t_0 + t_{stim} \end{cases} \tag{A.2}$$

where:

$$s_{up}(t) = \frac{s^*}{2}\left[1 + \mathrm{erf}\left(\frac{t - \left[t_0 + \tau_{up}/2\right]}{\sqrt{32}\tau_{up}}\right)\right]; \tag{A.3}$$

$$s_{down}(t) = s^* \exp\left(\frac{t_0 + t_{stim} - t}{\tau_{down}}\right); \tag{A.4}$$

t_0 is the stimulus onset time; τ_{up} and τ_{down} are time constants; t_{stim} is the duration of stimulation (where $t_{stim} \ge \tau_{up}$); s^* is the steady state value of the stimulus; and erf is the Gauss error function:

$$\mathrm{erf}(x) = \frac{2}{\pi}\int_0^x \exp\left(-t^2\right) dt\,. \tag{A.5}$$

For each of the stimulus intensities, the parameters defining the optimal imposed $CMRO_2$ increase (τ_{up}, s^*, and τ_{down}) are listed in Supplementary Table 3.

Tables

Table 1: List of dynamic variables.

Symbol	**Description**
$c_i(t)$	Vascular compliance
$c_{O_2,i,j}(t)$	O_2 concentration of $f_{i,j}(t)$
$\Delta c^{\text{å}}_{HbO}(t)\,;\ \Delta c^{\text{å}}_{dHb}(t)$	Adjusted haemoglobin concentration changes
$cmr_{O_2}(t)$	Cerebral metabolic rate of O_2
$f_{i,j}(t)\,;\ \overline{f}(t)$	Blood flow from *i* to *j*; average flow
$j_{O_2,i}(t)\,;\ j_{O_2,s}(t)$	O_2 flux to tissue; flux through shunt
$n_{X,i}(t)$	Amount of X, where $X \in \{O_2, HbO,\ \ldots\}$
$p_i(t)\,;\ \Delta p_i(t)$	Entrance fluid pressure; fluid pressure drop
$p_{O_2,i,j}(t)\,;\ \overline{p}_{O_2,i}(t)$	O_2 partial pressure of $f_{i,j}(t)$; average PO_2
$r_i(t)$	Viscous resistance
$s_{O_2,i}(t)$	O_2 saturation
$v_i(t)$	Blood volume

Figures

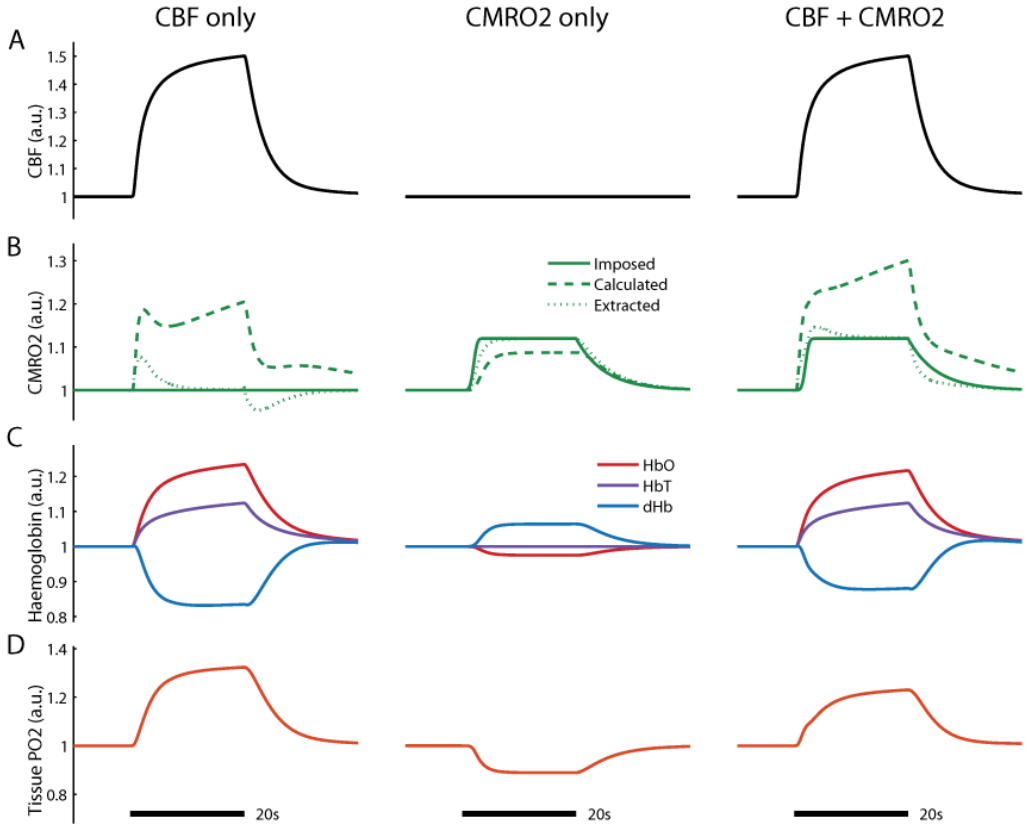

Figure 1: Comparison of the cerebral metabolic rate of oxygen ($CMRO_2$) directly imposed on the model and $CMRO_2$ calculated from haemoglobin predictions. Model predictions of (**A**) cerebral blood flow (CBF); (**B**) $CMRO_2$; (**C**) oxy (HbO), deoxy (dHb) and total (HbT) haemoglobin; and (**D**) tissue oxygen partial pressure (PO_2) in response to 20 second stimulation (scale bars on bottom row). Predictions are shown under three conditions: CBF increase only (left column); $CMRO_2$ increase only (middle column); and increases in both CBF and $CMRO_2$ (right column). Imposed, calculated and extracted $CMRO_2$ increases are calculated as per Equation (16) in the main text.

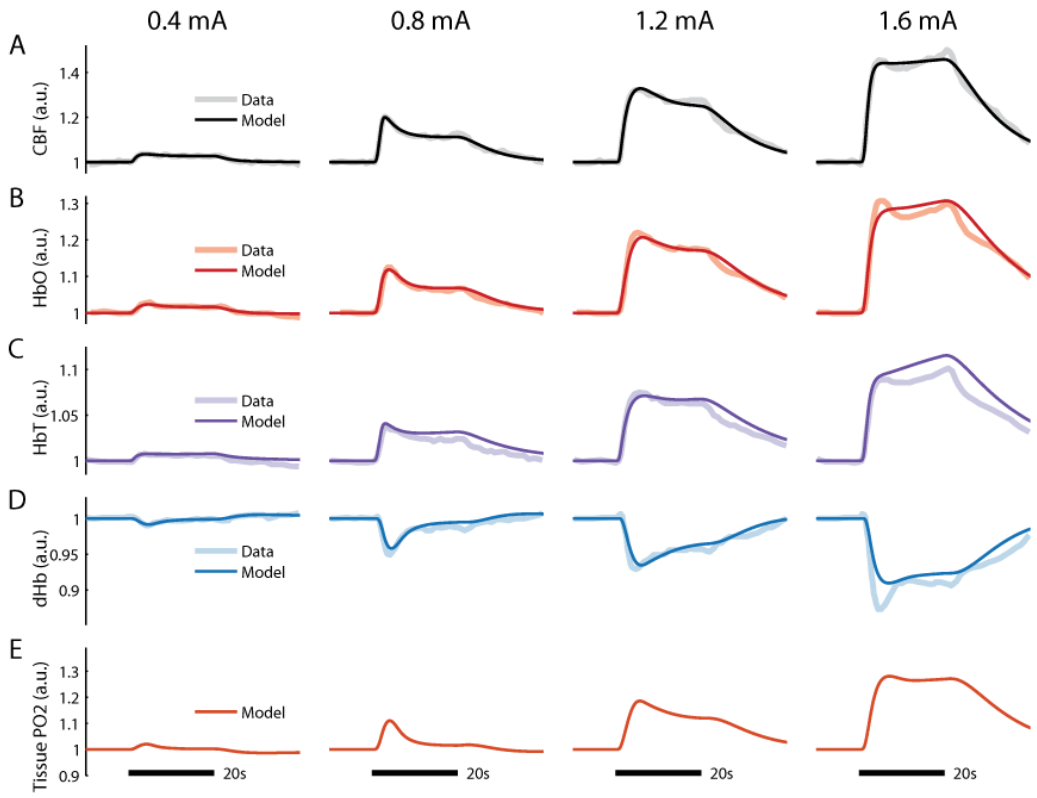

Figure 2: Model predictions fit to *in vivo* data from Jones *et al.* (2002). Optimal predictions of (**A**) cerebral blood flow (CBF); (**B**) oxy (HbO), (**C**) total (HbT) and (**D**) deoxyhaemoglobin (dHb); and (**E**) tissue oxygen partial pressure (PO_2) in response to 20 second stimulation (scale bars below bottom row). Stimulus intensities are graded from 0.4 (far left column) to 1.6 (far right column) milliamps (mA). Model predictions of oxy and deoxyhaemoglobin are adjusted to match the assumed baseline values (see main text and Supplementary Figures 1 and 2).

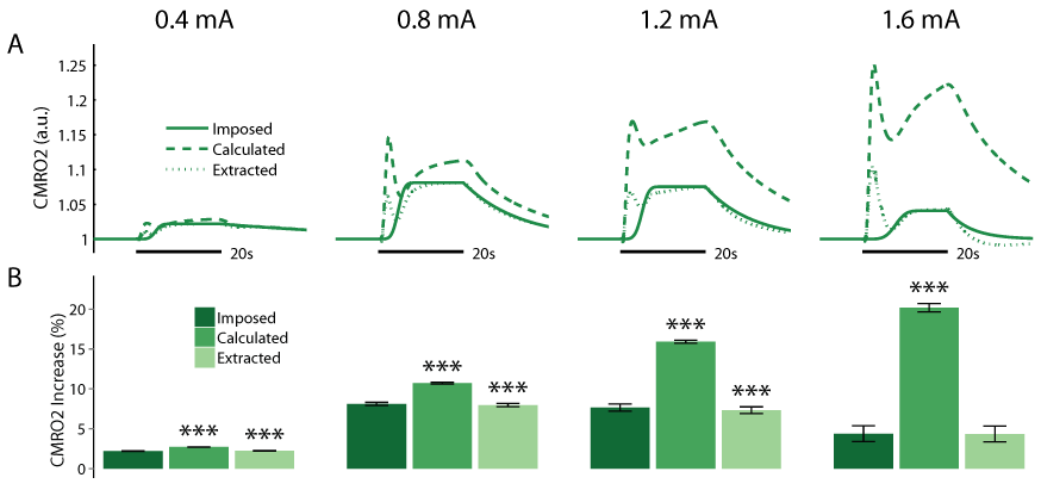

Figure 3: Estimates of cerebral metabolic rate of oxygen ($CMRO_2$) from the simulations of *in vivo* data shown in Figure 2. (**A**) Solid lines: dynamic $CMRO_2$ imposed on the model to achieve optimal fit to the data; dashed lines: $CMRO_2$ calculated from haemoglobin predictions; dotted lines: rate of O_2 extraction from blood to tissue. $CMRO_2$ estimates are calculated as per Equation (16) in the main text. (**B**) Increases in $CMRO_2$ during the plateau phase (see Figure 4) from all simulations in the sensitivity analysis (n = 36 simulations for each stimulus intensity; shown as mean ± s.d.; *** where $P < 0.001$ vs imposed $CMRO_2$). Stimulus intensities are graded from 0.4 (far left column) to 1.6 (far right column) milliamps (mA). The parameters defining the imposed $CMRO_2$ increase are listed in Supplementary Table 3.

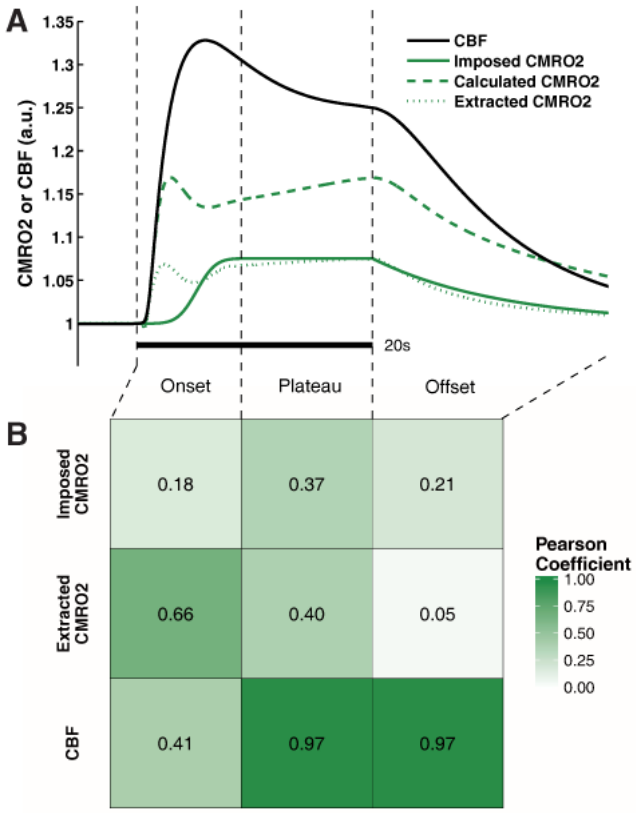

Figure 4: Correlation between other state variables and cerebral metabolic rate of oxygen ($CMRO_2$) calculated from blood flow and haemoglobin predictions. (**A**) Representative simulation showing dynamic predictions of cerebral blood flow (CBF) and estimates of imposed, calculated, and extracted $CMRO_2$ calculated as per Equation (16) in the main text. Dashed vertical lines divide the stimulation into three phases. (**B**) Pearson correlation coefficients calculated between calculated $CMRO_2$ and the other state variables. Correlation coefficients are calculated separately for the three stimulus phases by pooling a sample of data points (n = 8) from all sensitivity analysis simulations (n = 36) and all stimulus intensities (n = 4). The raw data are plotted in Supplementary Figure 3, and correlation coefficients calculated separately for each stimulus intensity are shown in Supplementary Figure 4.

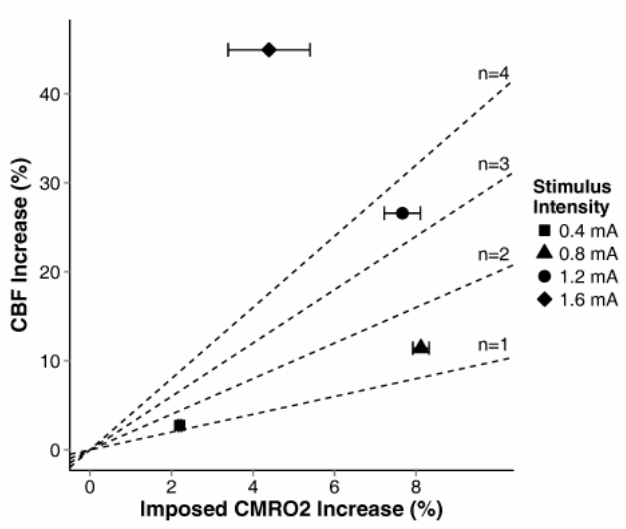

Figure 5: 'Coupling' between increases in cerebral blood flow (CBF) and cerebral metabolic rate of oxygen ($CMRO_2$) imposed on the model (as per Equation (16) in the main text). The data are pooled from all sensitivity analysis simulations (n = 36 for each stimulus intensity; shown as mean ± s.d.). Dashed lines are contours of constant coupling ratio n = $\Delta CBF/\Delta CMRO_2$.

Supplementary Table 1: List of model parameters in the reference state. Parameters with three values represent $x = [x_1, x_2, x_3]$, while parameters with four values represent $x = [x_{0,1}, x_{1,2}, x_{2,3}, x_{3,4}]$. Parameters with lower case symbols are dimensionless, while parameters with upper case symbols are not and are given with appropriate units.

Symbol	Description	Value	Reference
$C_{O_2,l}$	O_2 conc. leakage	0.116 mM	1
$C_{O_2,max}$	Hill equation max. O_2 conc.	9.26 mM	2
prop(g_s)	Proportion of shunt feasible range	50%	1
h	Hill equation exponent	2.6	2
P_{50}	Hill equation O_2 P_{50}	36 mmHg	2
$p^{\star}_{O_2,0}$	Experimental femoral artery PO_2	94.4 mmHg	3
$p^{*}_{O_2,0}$	Reference state femoral artery PO_2	85.6 mmHg	4
$p^{*}_{O_2}$	Reference state baseline vascular PO_2	[81.2, 59.7, 39.6, 41.3] mmHg	4
$p^{*}_{O_2,t}$	Reference state baseline tissue PO_2	22.4 mmHg	4
r^{*}	Baseline vascular resistance fraction	[0.74, 0.08, 0.18]	5
$[R_1, R_2]$	Krogh cylinder radii	[15, 135] μm	1
v^{*}	Baseline vascular volume fraction	[0.29, 0.44, 0.27]	5
v_t	Tissue volume fraction	34.8	1
w_b	Vascular PO_2 weight	0.133	1
w_i'	Vascular compartment weight	v^{*}	1
κ	Vascular stiffness coefficient	[1.29, 1.51, ∞]	5
ν	Vascular viscoelasticity coefficient	[31, 163, 122]	5
σ_{O_2}	Tissue O_2 solubility coefficient	1.46 μm/mmHg	6

Supplementary Table 2: List of parameters modified in the sensitivity analysis simulations and the amount of perturbation imposed. For parameters with multiple values (e.g. $p^*_{O_2}$), each value was perturbed individually.

Parameter	**Perturbation**
κ	±10%
ν	±10%
$p^*_{O_2}$	±10%
$[R_1, R_2]$	±10%
prop(g_s)	±40%
v^*	±10%
v_t	±10%
$p^\star_{O_2,0}$	±10%

Supplementary Table 3: List of parameters defining the imposed $CMRO_2$ increase for the simulations presented in Figure 3 in the main text. The parameters are described in more detail in Appendix A in the main text.

Stimulus	τ_{up} **(s)**	s^* **(a.u.)**	τ_{down} **(s)**
0.4 mA	9.0	0.022	40.0
0.8 mA	9.3	0.081	13.2
1.2 mA	10.1	0.075	11.1
1.6 mA	15.6	0.041	5.5

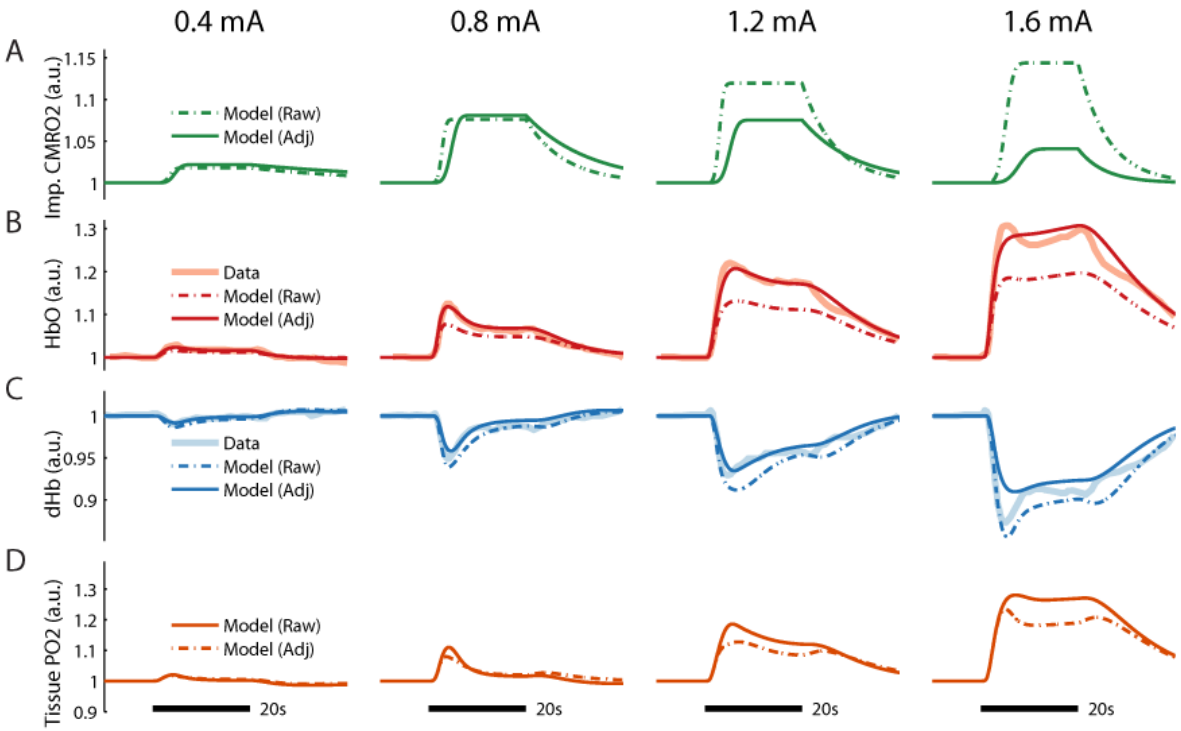

Supplementary Figure 1: Comparison of dynamic raw model predictions and predictions adjusted to match the assumed baseline values, both fit to *in vivo* data from Jones *et al.* (2002). Optimal predictions of: (**A**) cerebral metabolic rate of oxygen imposed on the model (Imp. CMRO2), as per Equation (16) in the main text; (**B**) oxy (HbO) and (**C**) deoxyhaemoglobin; and (**D**) tissue oxygen partial pressure (PO_2) in response to 20 second stimulation (scale bars below bottom row). Stimulus intensities are graded from 0.4 (far left column) to 1.6 (far right column) milliamps (mA). Adjusted HbO and dHb predictions are calculated from raw predictions using Equation (16) in the main text. A summary of results from all simulations in the sensitivity analysis is shown in Supplementary Figure 2.

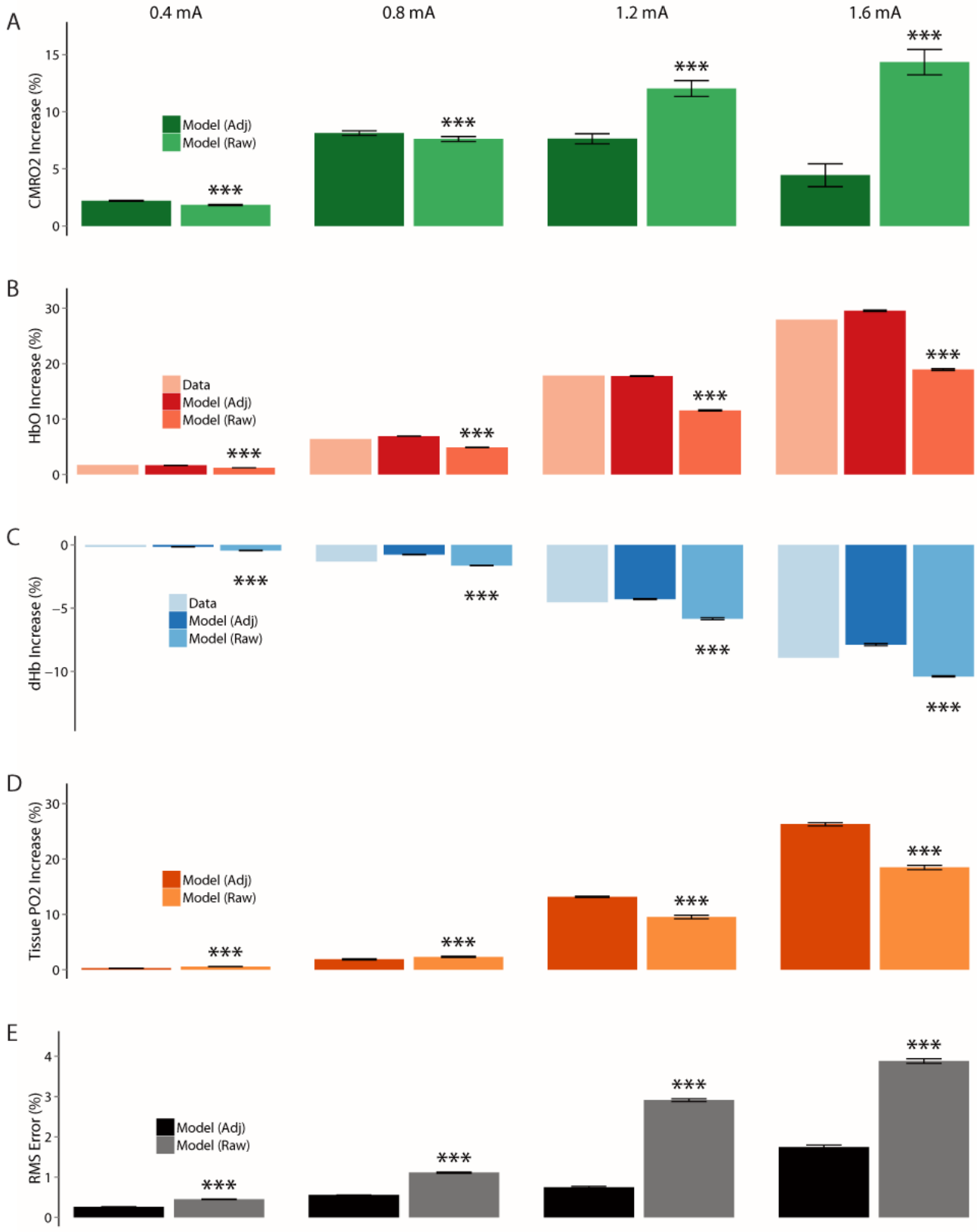

Supplementary Figure 2: Summary of raw model predictions and predictions adjusted to match the assumed baseline values, both fit to *in vivo* data from Jones *et al.* (2002). Increases of: (**A**) cerebral metabolic rate of oxygen ($CMRO_2$) imposed on the model, as per Equation (16) in the main text; (**B**) oxy (HbO) and (**C**) deoxyhaemoglobin; (**D**) tissue oxygen partial pressure (PO_2); and (**E**) root mean square (RMS) error from all simulations in the sensitivity analysis (n = 36 simulations for each stimulus intensity; shown as mean ± s.d.; *** where $P < 0.01$ vs adjusted metrics). Stimulus intensities are graded from 0.4 (far left column) to 1.6 (far right column) milliamps (mA). Adjusted HbO and dHb predictions are calculated from raw predictions using Equation (16) in the main text.

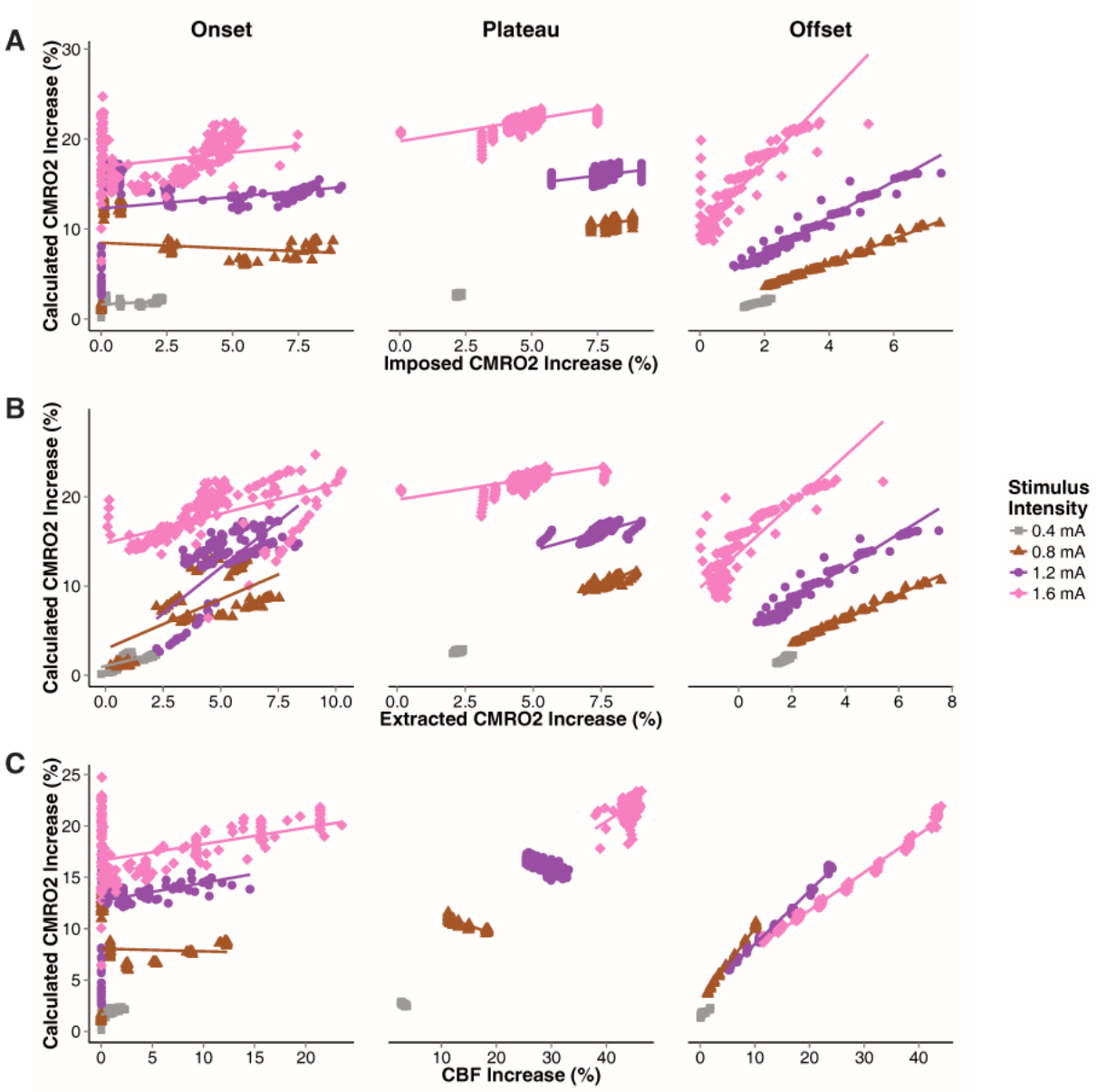

Supplementary Figure 3: Raw data used to calculate correlation between other state variables and cerebral metabolic rate of oxygen ($CMRO_2$) calculated from haemoglobin predictions as per Equation (16) in the main text. Increases in calculated $CMRO_2$ are plotted against: (**A**) $CMRO_2$ increases imposed on the model; (**B**) rate of oxygen extraction from blood to tissue; and (**C**) cerebral blood flow (CBF). Each plot contains data points (n = 8) from each of the simulations in the sensitivity analysis (n = 36) at each of the stimulus intensities (n = 4). The correlation coefficients calculated by pooling data from all stimulus intensities are shown in Figure 4, and coefficients calculated separately for each stimulus intensity level are shown in Supplementary Figure 4.

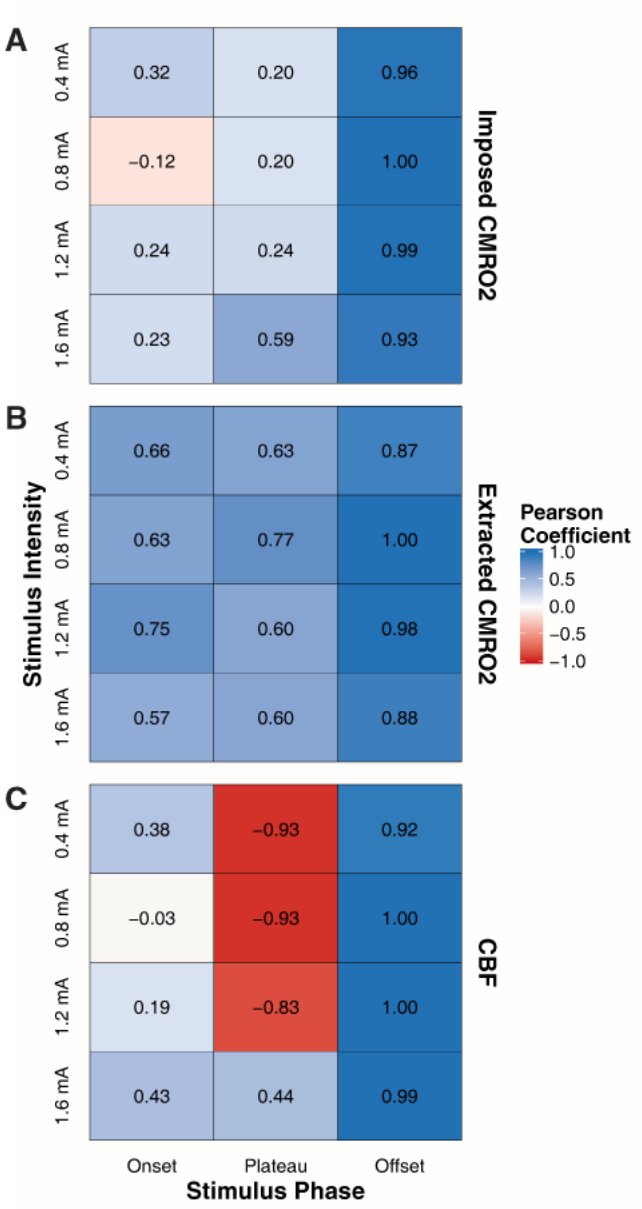

Supplementary Figure 4: Correlation between cerebral metabolic rate of oxygen ($CMRO_2$) calculated from haemoglobin predictions as per Equation (16) in the main text and: (**A**) $CMRO_2$ imposed on the model; (**B**) $CMRO_2$ extracted from blood to tissue; and (**C**) cerebral blood flow (CBF). Correlation coefficients are calculated separately for the three stimulus phases and each of the four stimulus intensities by pooling a sample of data points (n = 8) from all sensitivity analysis simulations (n = 36). The raw data are plotted in Supplementary Figure 3 and correlation coefficients calculated by pooling data from all stimulus intensities are shown in Figure 4.

Supplementary References

1. Barrett MJP, Suresh V. Extra permeability is required to model dynamic oxygen measurements: evidence for functional recruitment? *J. Cereb. Blood Flow Metab.* 2013**:** 1-10.

2. Cartheuser C-F. Standard and pH-affected hemoglobin-O2 binding curves of Sprague-Dawley rats under normal and shifted P50 conditions. *Comp. Biochem. Physiol. A.* 1993; **106**(4)**:** 775 - 782.

3. Jones M, Berwick J, Mayhew J. Changes in Blood Flow, Oxygenation, and Volume Following Extended Stimulation of Rodent Barrel Cortex. *Neuroimage* 2002; **15**(3)**:** 474 - 487.

4. Vovenko E. Distribution of oxygen tension on the surface of arterioles, capillaries and venules of brain cortex and in tissue in normoxia: an experimental study on rats. *Pflugers Arch.* 1999; **437**(4)**:** 617-623.

5. Barrett MJP, Tawhai MH, Suresh V. Arteries dominate volume changes during brief functional hyperemia: Evidence from mathematical modelling. *Neuroimage* 2012; **62**(1)**:** 482 - 492.

6. Dash R, Bassingthwaighte J. Blood HbO2 and HbCO2 Dissociation Curves at Varied O2, CO2, pH, 2,3-DPG and Temperature Levels. *Ann. Biomed. Eng.* 2004; **32**(12)**:** 1676-1693.